Applied Catalysis B: Environment and Energy 384 (2026) 126158

Contents lists available at ScienceDirect

Applied Catalysis B: Environment and Energy

journal homepage: www.elsevier.com/locate/apcatb

Lattice strain induced $Ni_{0.85}Se/WO_{2.90}$ heterostructures accelerate dynamic reconstruction for efficient water oxidation

Qimin Peng [a,b,1], Jianqiu Zhu [c,1], Fengli Wei [a], Tayirjan Taylor Isimjan [d], Tianxiao Sun [e,*], Xiulin Yang [a,*], Yongfa Zhu [f,*], Bin Wu [g,*]

[a] Guangxi Key Laboratory of Low Carbon Energy Materials, School of Chemistry and Pharmaceutical Sciences, Guangxi Normal University, Guilin, Guangxi 541004, China
[b] College of materials science and engineering, Beijing University of Chemical Technology, Beijing 100029, China
[c] Key Laboratory of Interfacial Physics and Technology, Shanghai Institute of Applied Physics, Chinese Academy of Sciences, Shanghai 201008, China
[d] Saudi Arabia Basic Industries Corporation (SABIC) at King Abdullah University of Science and Technology (KAUST), Thuwal, 23955-6900, Saudi Arabia
[e] Walker Department of Mechanical Engineering, The University of Texas at Austin, Austin, TX 78712, USA
[f] Department of Chemistry, Tsinghua University, Beijing 100084, China
[g] School of Materials Science and Engineering, Nanyang Technological University, 50 Nanyang Avenue, Singapore 639798, Singapore

ARTICLE INFO

Keywords:
$Ni_{0.85}Se/WO_{2.90}$
Heterostructure
Oxygen vacancy
Oxygen evolution reaction
Overall water splitting

ABSTRACT

Constructing heterostructure catalysts with rich defects and lattice distortions is an efficient strategy to enhance the activity of electrocatalysts, and identifying true active sites *in-situ* is also a major challenge in water electrolysis. Herein, an oxygen-rich vacancy heterostructure ($Ni_{0.85}Se/WO_{2.90}$) is fabricated *via* three-step route, which is provided with an extraordinary oxygen evolution activity in alkaline solution, achieving low overpotentials of 230/295 mV at current densities of 20/100 mA cm^{-2}, respectively. And a small Tafel slope of 40.6 mV dec^{-1} indicating favorable reaction kinetics. Besides, it shows outstanding long-term stability, maintaining its performance for 100 h at 20 mA cm^{-2} with negligible degradation. Besides, only a cell voltage of 1.76 V is needed to offer 100 mA cm^{-2} by the assembled $Ni_{0.85}Se/WO_{2.90}||Pt/C$ electrolyzer. *In situ* studies reveal that $Ni_{0.85}Se$ undergoes dynamic reconstruction into active NiOOH species during operation. Meanwhile, W stabilizes in the form of W-O within $WO_{2.90}$ matrix. The abundant oxygen vacancies and lattice distortions synergize with adjacent sites. This synergy optimizes the adsorption/desorption energetics for oxygen intermediates, thereby dramatically accelerating the oxygen evolution reaction (OER) kinetics. This strong alignment of experimental and theoretical results highlights the potential of $Ni_{0.85}/WO_{2.90}$ as a leading candidate for water oxidation applications.

1. Introduction

The ongoing reliance on fossil fuels and the resultant rise in carbon emissions have intensified research into renewable energy technologies. To date, the electrochemical conversion of renewable resources into electricity and fuels stands out as a pivotal approach towards clean energy [1–4]. The overarching technique of water splitting through electrochemistry is viewed as pivotal for producing green hydrogen, a versatile energy carrier and a foundational element for energy storage and chemical industry inputs. This process incorporates the oxygen evolution reaction (OER) at the anode and the hydrogen evolution reaction (HER) at the cathode [5–7]. Currently, the overall efficiency of the water electrolysis process is principally restricted by the high energy consumption caused from the overpotential of the OER half-reaction, which involves the complex and sluggish multistep proton-coupled electron transfer process and O-O bond formation [8–10]. As a result, accelerating the research of reaction kinetics and fundamental understanding of OER are imperiously demanded to achieve energy-efficient water oxidation. Whereas, the significant hindrance of water electrolysis is the reliance on scarce, expensive, and unstable noble metals like Pt, IrO_2, and RuO_2.

The development of affordable and abundant transition metal-based

* Corresponding authors.
E-mail addresses: tianxiao.sun@utexas.edu (T. Sun), xlyang@gxnu.edu.cn (X. Yang), zhuyf@tsinghua.edu.cn (Y. Zhu), bin.wu@ntu.edu.sg (B. Wu).
[1] State Key Laboratory of Chemical Resource Engineering, Beijing Key Laboratory of Electrochemical Process and Technology of Materials, National Engineering Research Center for Fuel Cell and Hydrogen Source Technology, Beijing University of Chemical Technology, Beijing 100029, P.R. China.

https://doi.org/10.1016/j.apcatb.2025.126158
Received 12 October 2025; Received in revised form 29 October 2025; Accepted 4 November 2025
Available online 5 November 2025

electrocatalysts that offer similar activity and stability is, therefore, imperative. Recent studies have made significant strides in designing 3*d* transition metal-based materials, with OER catalysts comprising various compositions including selenides [11,12], oxides [13,14], hydroxides [15,16], and phosphates [17], etc. One promising approach is to construct heterostructures that combine two or more components. The advantage is that these heterostructures can combine the strengths and offset the weaknesses of each individual component, optimizing their structure and electronic characteristics to enhance OER performance [18,19]. Specifically, these structures can promote electron rearrangement and active site exposure, leading to a reduction in the OER's energy barrier [20–22].

While the idea of heterostructure engineering is conceptually simple, the choice of components for a specific purpose requires careful consideration. Notably, recent nickel-based heterostructures, for instance NiO/Co_3O_4 [23], MoS_2/NiS_2 [24], $NiS_2/NiSe_2$ [25], $FeS_2@NiS_2$ [26], Ni_3Sn_2-$NiSnO_x$ [27], etc, which have demonstrated efficient OER performance thanks to their chemically adjustable structures. Still, the challenge remains to identify new nickel-based electrocatalysts through straightforward synthesis methods. Leveraging defects and lattice strain in heterostructures can amplify their catalytic properties. Given tungsten oxide's unique redox and Lewis acid/base attributes [28,29], it offers robust interactions with other active components, aiding both in optimizing the activity of active substances and stabilizing substrates. Oxygen-deficient tungsten oxide also enhances hydrolysis kinetics, speeding up O_2 release. Thus, this study proposes a catalyst modified by $WO_{2.90}$ on a $Ni_{0.85}Se$ base, aiming to enhance catalytic performance and stability. Additionally, research indicates that OER pre-catalysts undergo structural transformations in alkaline solutions, resulting in the creation of metal-based (oxy)hydroxides (MOOH) as the real catalytic agents [30–32]. Therefore, a thorough understanding of these transformation behaviors is crucial for designing effective catalysts [33–35].

In our study, we developed a catalyst featuring $Ni_{0.85}Se$ nanoparticles anchored to a $WO_{2.90}$ nanowire structure with a high oxygen vacancy content. This composition showcased exceptional OER efficiency and stability in an alkaline solution. When paired with Pt/C in a water electrolyzer, the catalyst required a mere 1.53 V to achieve a 20 mA cm^{-2} output. This superior performance is largely attributed to the composite's large active surface area and oxygen-rich vacancies, ensuring effective electron transfer. Both experimental and DFT calculations show that the designed $Ni_{0.85}Se/WO_{2.90}$, with its induced lattice distortion, can enhance conductivity, aid electron transfer, and lower the energy barrier of the rate-determining step, significantly boosting electrocatalytic activity. This research offers a viable design pathway for non-precious metal OER catalysts vital for future renewable energy applications.

2. Experimental sections

2.1. Materials

All reagents and chemicals were commercially available and without further purification. Nickel nitrate hexahydrate ($Ni(NO_3)_2{\cdot}6\ H_2O$, 99.0 %), selenium powder (Se, 99.99 %), tungsten hexachloride (WCl_6, 98.0 %), potassium hydroxide (KOH, 90.0 %), ethanol (C_2H_5OH, 99.7 %), hydrazine hydrate ($N_2H_4{\cdot}H_2O$, 80 %), Pluronic P123, hydrochloric acid (HCl, 37.0 %). Carbon cloth (CC) was purchased from commercial company. The 5 wt% Nafion solution and commercial Pt/C (20 wt% for platinum) were all purchased from Adamas Chemical Reagent Co. Ltd. The deionized water (18.2 MΩ cm^{-2}) was produced by an ultrapure water system (Millipore).

2.2. Preparation of $NiSeO_3{\cdot}3\ H_2O$

In a typical synthesis of the $NiSeO_3{\cdot}3\ H_2O$, 0.1579 g selenium powder was firstly dissolved in 4 mL hydrazine hydrate with stirring for 30 min. Then 0.5816 g $Ni(NO_3)_2{\cdot}6\ H_2O$, 300 mg Pluronic P123, 15 mL water and 15 mL ethanol were added. The mixture was kept stirring at room temperature for 12 h. The resulting black precipitates were collected by centrifugation, washed with water and ethanol three times, and finally dried at 60 ℃ overnight.

2.3. Preparation of $NiSe_2/WO_{2.90}$

Typically, 100 mg WCl_6 was dissolved in 10 mL water and 10 mL ethanol with stirring for 30 min, and then the as-prepared $NiSeO_3{\cdot}3\ H_2O$ (100 mg) was added in the above solution. The mixture was kept stirring at room temperature for 3 h. The obtained solution was then transferred to a Teflon-lined stainless steel autoclave and heated at 180 ℃ for 6 h. After natural cooling, the resulting dark gray precipitates were collected by centrifugation, washed with water and ethanol three times, and finally dried at 60 ℃ overnight.

2.4. Preparation of $Ni_{0.85}Se/WO_{2.90}$

The as-prepared $NiSe_2/WO_{2.90}$ was annealed at 380 ℃ for 2 h at a heating rate of 5 ℃ min^{-1} in H_2/Ar (10/90) atmosphere to obtain $Ni_{0.85}Se/WO_{2.90}$. Similarly, $NiSe_2/WO_{2.90}$-350 and $Ni_{0.85}Se/WO_{2.90}$-400 were prepared with the same method except for the calcination temperatures (350 and 400 ℃, respectively). A set of catalysts with various relative W loading were also prepared by varying the amount of WCl_6 (e.g.,50 and 200 mg), which were denoted $Ni_{0.85}Se/WO_{2.90}$-1/2 and $Ni_{0.85}Se/WO_{2.90}$-2.

2.5. Preparation of RuO_2 wt% Pt/C electrodes

The commercial $RuCl_3{\cdot}3\ H_2O$ was directly calcined at 400 °C for 3 h in the air to obtain RuO_2 powders. And then 2 mg RuO_2 or 20 wt% commercial Pt/C was dispersed into a mixture of 200 μL deionized water, 200 μL ethanol and 10 μL 5 wt% Nafion, respectively. The mixture was ultrasonically treated for at least 30 min to form a uniform catalyst ink, then dropped onto the surface of CC (1 cm × 1 cm) and dried naturally in the air.

3. Results and discussion

3.1. Analysis of oxygen vacancies structure and lattice strain

The synthesis of $Ni_{0.85}Se/WO_{2.90}$ heterostructure material with oxygen-rich vacancies was accomplished using a simple method. This involved a room temperature coprecipitation, followed by a hydrothermal reaction and reduction treatments using a H_2/Ar mixture, as depicted in Fig. 1a. The process began with the creation of $NiSeO_3{\cdot}3\ H_2O$ nanoparticles using coprecipitation (Fig. S1). These nanoparticles subsequently served as a template to absorb W ions from a solution. The final catalyst, rich in oxygen vacancies, was obtained through calcination.

To evaluate the structure and morphology of $Ni_{0.85}Se/WO_{2.90}$, both scanning electron microscopy (SEM) and transmission electron microscopy (TEM) were utilized. The SEM (Fig. 1b) alongside TEM images at low magnification (Fig. 1c and Fig. S2) highlighted the distinctive urchin-like structure of $Ni_{0.85}Se/WO_{2.90}$. This structure was seen to be evenly coated with numerous nanoparticles. Structures of this kind have been associated with beneficial properties in electrocatalysis, such as generating more defects, offering a multitude of accessible active sites, and promoting shorter electron/ion and gas evolution pathways [36,37]. The high-resolution TEM (HRTEM) image of $Ni_{0.85}Se/WO_{2.90}$ presented in Fig. 1d unveiled further structural details. Notably, the measured spacings between consecutive lattice fringes, 0.374 nm and 0.290 nm, correlate well with the (110) plane of tetragonal $WO_{2.90}$ and the (101) plane of hexagonal $Ni_{0.85}Se$, respectively. This observation is corroborated by the selected area electron diffraction (SAED) pattern

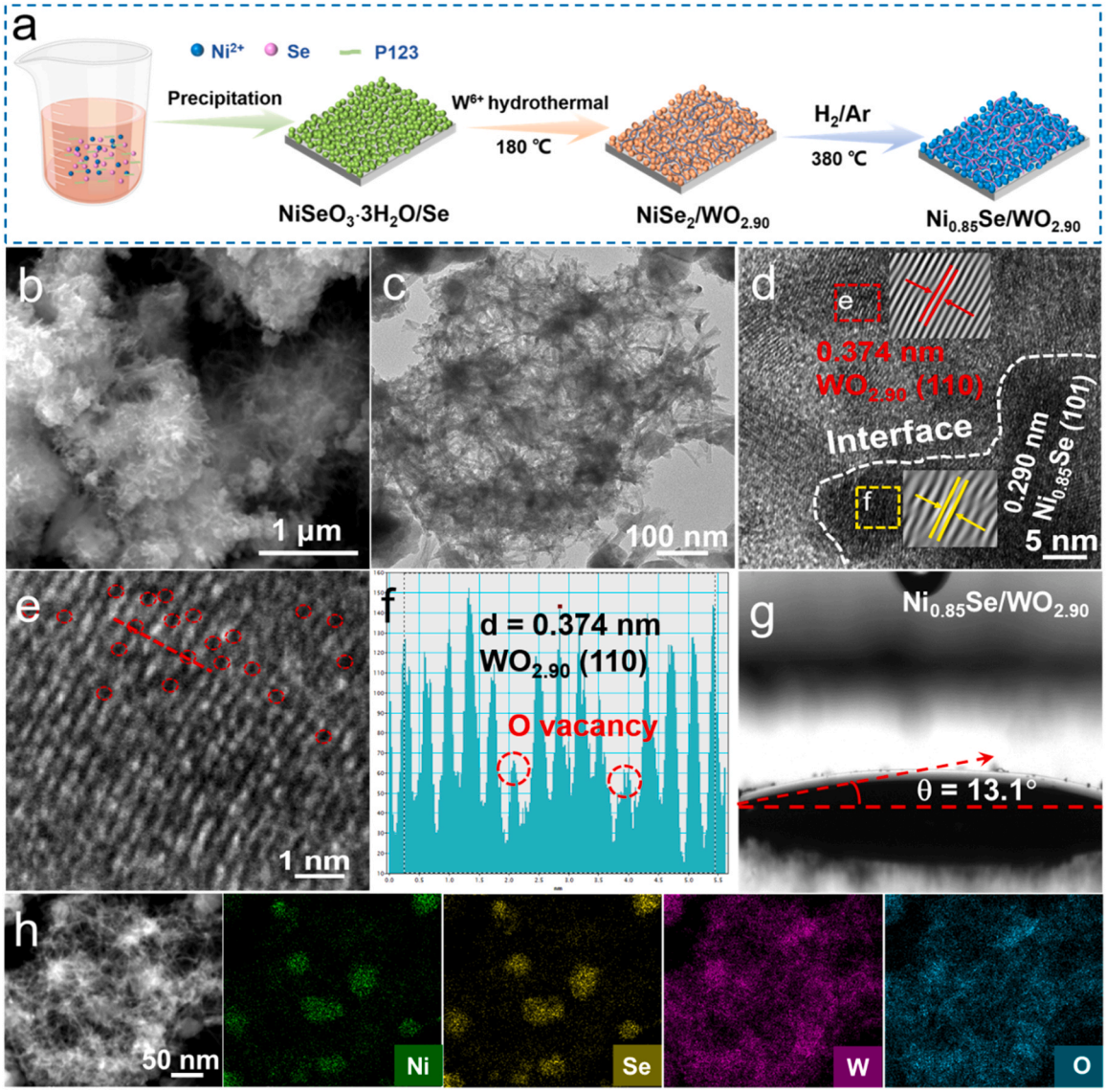

Fig. 1. Fabrication and characterization of $Ni_{0.85}Se/WO_{2.90}$. (a) Preparation scheme. (b) SEM image. (c) TEM image. (d) High-resolution TEM (HRTEM) image. (e-f) The magnified HRTEM of the corresponding region. (g) Water contact angle test on the surface of the as-prepared catalyst. (h) HAADF-STEM and related elemental mapping images in $Ni_{0.85}Se/WO_{2.90}$.

(Fig. S2), which distinctly shows diffraction rings related to these planes [38,39].

As marked by red circles in Fig. 1e, reveals abundant anionic oxygen vacancies in the HRTEM images. The intensity profile within the framed area (inset of Fig. 1e) lends further support to the presence of these oxygen vacancies in the $Ni_{0.85}Se/WO_{2.90}$ catalyst. An enlarged version of the HRTEM image (Fig. 1f) illustrates the evident lattice distortion, a sign of the alteration of the host's original crystalline structure due to the introduction of $WO_{2.90}$. Importantly, such lattice defects are known to enhance the oxygen evolution reaction (OER) performance, particularly by augmenting the adsorption capacity of reaction intermediates [40].

Furthermore, the energy dispersive X-ray spectrum (EDX) confirms the presence of Ni, W, Se, and O elements in the sample (Figs. S2-4). The elemental mapping of $Ni_{0.85}Se/WO_{2.90}$ exhibits a clear pattern: Ni and Se elements are evenly distributed across the nanoparticles found on the surface of the urchin-like structure, whereas W and O are uniformly distributed throughout the entire urchin structure, lending further evidence to the formation of this distinctive urchin morphology (depicted in Fig. 1h). Beyond structural considerations, other properties like electrical conductivity and hydrophilicity play pivotal roles in improving both electron and mass transfer. To gain insight into how the interfacial ion/molecule interactions influence water adhesion, we conducted contact angle tests on all the synthesized materials. Results visible in Fig. 1g and Fig. S5, show that $Ni_{0.85}Se/WO_{2.90}$ exhibits a particularly high hydrophilic nature, with a static contact angle of just 13.1°. This is notably lower when compared to $NiSe_2/WO_{2.90}$ (with a contact angle of 21.4°), $NiSeO_3{\cdot}3\,H_2O$ (37.8°), $WO_{2.90}$ (36.2°), and $Ni_{0.85}Se$ (25.1°). This heightened hydrophilicity can be credited to the distinctive urchin-like structure of the material.

This enhanced surface wettability translates to improved kinetics for $NiSe_2/WO_{2.90}$, promoting both hydroxyl oxidation kinetics and the O-O bond coupling process both essential for the OER reaction. Furthermore, the unique urchin-like nanostructure not only enhances hydrophilicity (allowing for better penetration of the electrolyte into active sites) but also ensures that gas bubbles are kept at a distance from the catalyst surface. Both these factors combined result in an augmentation of the catalytic activity during the OER process.

The crystalline characteristics of the synthesized samples were validated through powder X-ray diffraction (XRD) tests. In the composite

material, diffraction peaks observed at 33.15°, 44.95°, 50.49°, and 60.24° can be aligned with the (101), (102), (110), and (103) planes of the hexagonal $Ni_{0.85}Se$ structure (JCPDS: 18–0888) [41]. Simultaneously, peaks at 23.77°, 33.80°, 54.94°, and 60.46° correspond to the (110), (200), (310), and (311) planes of the tetragonal $WO_{2.90}$ (JCPDS: 18–1417) (Fig. 2a and Figs. S6-8). The Ni/W molar ratios, as determined by inductively coupled plasma atomic emission spectrometry (ICP-AES), align well with the initial feed ratios (Table S1). In the Raman spectra depicted in Fig. 2b, characteristic peaks positioned at 262, 683, and 980 cm^{-1} are identifiable as stemming from nickel selenides [25]. Further insight into the density of oxygen defects in $Ni_{0.85}Se/WO_{2.90}$ is provided by the electron paramagnetic resonance (EPR) spectra. Here, the EPR signal, pinpointed at a value of 2.003, is indicative of electrons confined within oxygen vacancies, paralleling past research (Fig. 2c and Fig. S9) [42]. When contrasting the EPR signals, $Ni_{0.85}Se/WO_{2.90}$ stands out with a significantly enhanced and distinct signal compared to other samples. Such unusual lattice expansion observed in $Ni_{0.85}Se$ may be attributed to the creation of negatively charged anion vacancies, as confirmed by EPR- a phenomenon well-documented in prior studies [43]. These examinations collectively underscore that the $Ni_{0.85}Se/WO_{2.90}$ is enriched with oxygen vacancies, likely resulting from the H_2/Ar calcination process- an observation that dovetails with findings from the HRTEM. In oxide materials, a high concentration of oxygen vacancies can uncover more metal sites, thereby amplifying the count of active catalytic sites and consequently speeding up the reaction kinetics pivotal to the OER process [44].

The as-prepared samples' electronic states and chemical composition were probed using X-ray photoelectron spectroscopy (XPS). The XPS survey spectrum for $Ni_{0.85}Se/WO_{2.90}$ confirmed the presence of Ni, W, Se, and O elements (as seen in Fig. S10), aligning with the earlier EDX and ICP-AES observations. A deeper look at the high-resolution Ni 2*p* spectra of both $Ni_{0.85}Se/WO_{2.90}$ and $Ni_{0.85}Se$ (displayed in Fig. 2d) reveals two distinct regions: Ni $2p_{1/2}$ and Ni $2p_{3/2}$. These can further be split into three peak pairs. The predominant Ni 2*p* XPS peaks correspond to the typical spin-orbital peaks of Ni^{3+} and Ni^{2+}. Specifically, the bands for Ni $2p_{3/2}$ and Ni $2p_{1/2}$ at 853.2 and 870.8 eV, respectively, coupled with their satellite peaks at 860.3 and 879.4 eV, are indicative of Ni^{2+} in $Ni_{0.85}Se/WO_{2.90}$. Meanwhile, the peaks at 855.6 eV ($2p_{3/2}$) and 873.7 eV ($2p_{1/2}$) align with Ni^{3+} ions. Notably, a positive shift (roughly 0.25 eV) in the Ni^{2+} binding energies of $Ni_{0.85}Se/WO_{2.90}$ compared to $Ni_{0.85}Se$ alone indicates a change in electron distribution, likely driven by the interaction between $Ni_{0.85}Se$ and $WO_{2.90}$, with a slight shift to higher energy upon introducing lattice strain. For the W 4 *f* XPS spectrum (Fig. 2e), the two peaks at 36.0 and 38.2 eV match the W $4f_{7/2}$ and W $4f_{5/2}$ of W^{6+}, respectively. Moreover, two additional deconvoluted peaks at 34.7 and 36.9 eV can be associated with W^{5+}. Compared to pure $WO_{2.90}$, $Ni_{0.85}Se/WO_{2.90}$ showcases an increased W^{5+}/W^{6+} ratio and a distinct shift towards lower binding energy (0.25 eV). This indicates the partial reduction of W^{6+} to W^{5+}, in tandem with the growing content of oxygen vacancies and a reinforced electronic link between W and Ni

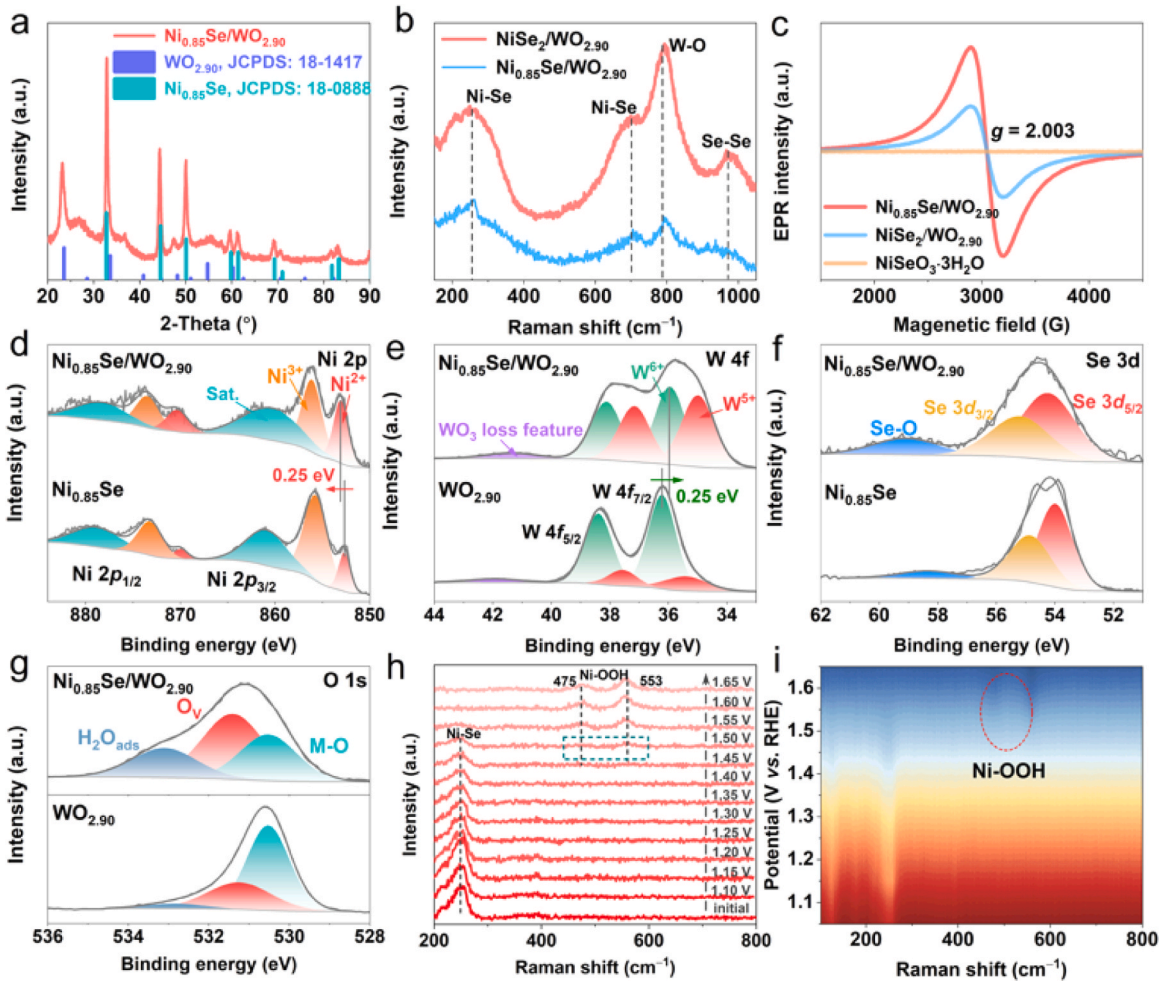

Fig. 2. Phase structure and chemical composition study of the catalysts. (a) XRD pattern of $Ni_{0.85}Se/WO_{2.90}$. (b) Raman spectra of $Ni_{0.85}Se/WO_{2.90}$ and $NiSe_2/WO_{2.90}$. (c) EPR spectra of $Ni_{0.85}Se/WO_{2.90}$, $NiSe_2/WO_{2.90}$, and $NiSeO_3{\cdot}3\,H_2O$. High-resolution XPS spectra of $Ni_{0.85}Se/WO_{2.90}$, $NiSe_2/WO_{2.90}$, $Ni_{0.85}Se$, and $WO_{2.90}$ (d) Ni 2*p*, (e) W 4 *f*, (f) Se 3*d*, and (g) O 1 *s*. (h) *In situ* Raman spectra of $Ni_{0.85}Se/WO_{2.90}$. (i) Contour plots of the *in situ* Raman spectra at different potentials (*vs.* RHE) in 1.0 M KOH.

(Figs. S11-13). Examining the Se 3*d* spectra reveals peaks at 54.2 and 55.3 eV, corresponding to Se $3d_{5/2}$ and Se $3d_{3/2}$, which originate from Se species bound to Ni^{2+}. A peak at 58.9 eV can be attributed to Se-O species, suggesting some surface oxidation (Fig. 2f). The O 1 *s* spectra (Fig. 2g) contain three deconvoluted peaks: 530.5 eV for metal oxygen (M-O), 531.7 eV for oxygen vacancies (O_v), and 533.0 eV for adsorbed water molecules (H_2O_{ads}). These further confirm the creation of oxygen vacancies. These XPS findings are harmonious with EPR and HRTEM results. Additionally, the oxygen vacancy percentage in $Ni_{0.85}Se/WO_{2.90}$ is found to be approximately 47.2 %, in line with the W^{5+} content deduced from the W 4 *f* XPS spectra.

Various studies have highlighted that the surfaces of Ni-based catalysts undergo transformation, specifically converting into layered (oxy) hydroxides (NiOOH) as nickel cations oxidize to higher valence states under strong oxidative OER potentials [45,46]. In order to both substantiate the operando reconstruction of our material and identify the genuine reactive intermediates, we employed potential-dependent in situ Raman spectroscopy. Alongside electrochemical testing, this allowed for the real-time observation of the catalyst's dynamic changes under OER conditions. The operando Raman spectrum, which monitored the intermediates at applied potentials ranging from the initial setting to 1.65 V for $Ni_{0.85}Se/WO_{2.90}$, is illustrated in Fig. 2h-i. The primary Raman spectrum of $Ni_{0.85}Se/WO_{2.90}$ showcased a distinctive peak near 262 cm^{-1}, which can be associated with the Ni-Se vibrations upon its submersion in 1.0 M KOH. However, as the applied voltage was incrementally increased to 1.50 V, the Ni-Se peaks almost entirely disappeared. This indicates that structural modifications transpired within the $Ni_{0.85}Se/WO_{2.90}$ catalyst upon the application of an oxidative potential. When this potential reached 1.5 V (relative to RHE), two pronounced Raman peaks emerged around 475 and 553 cm^{-1}. These can be ascribed to the bending and stretching vibration modes of Ni-O-O-H [47,48]. Interestingly, as the applied potential surged, these peaks not only emerged but also gained in intensity [49]. This suggests a gradual transformation of $Ni_{0.85}Se$ into NiOOH. This alteration implies that NiOOH, acting as the actual active phase, prompts a complete overhaul of the catalyst's surface during the process.

Furthermore, the formation of the $Ni_{0.85}Se/WO_{2.90}$ was further corroborated by X-ray absorption near-edge structure (XANES) and extended X-ray absorption fine structure (EXAFS) measurements. The Ni K-edge XANES spectra of the $Ni_{0.85}Se/WO_{2.90}$ and $Ni_{0.85}Se$ samples

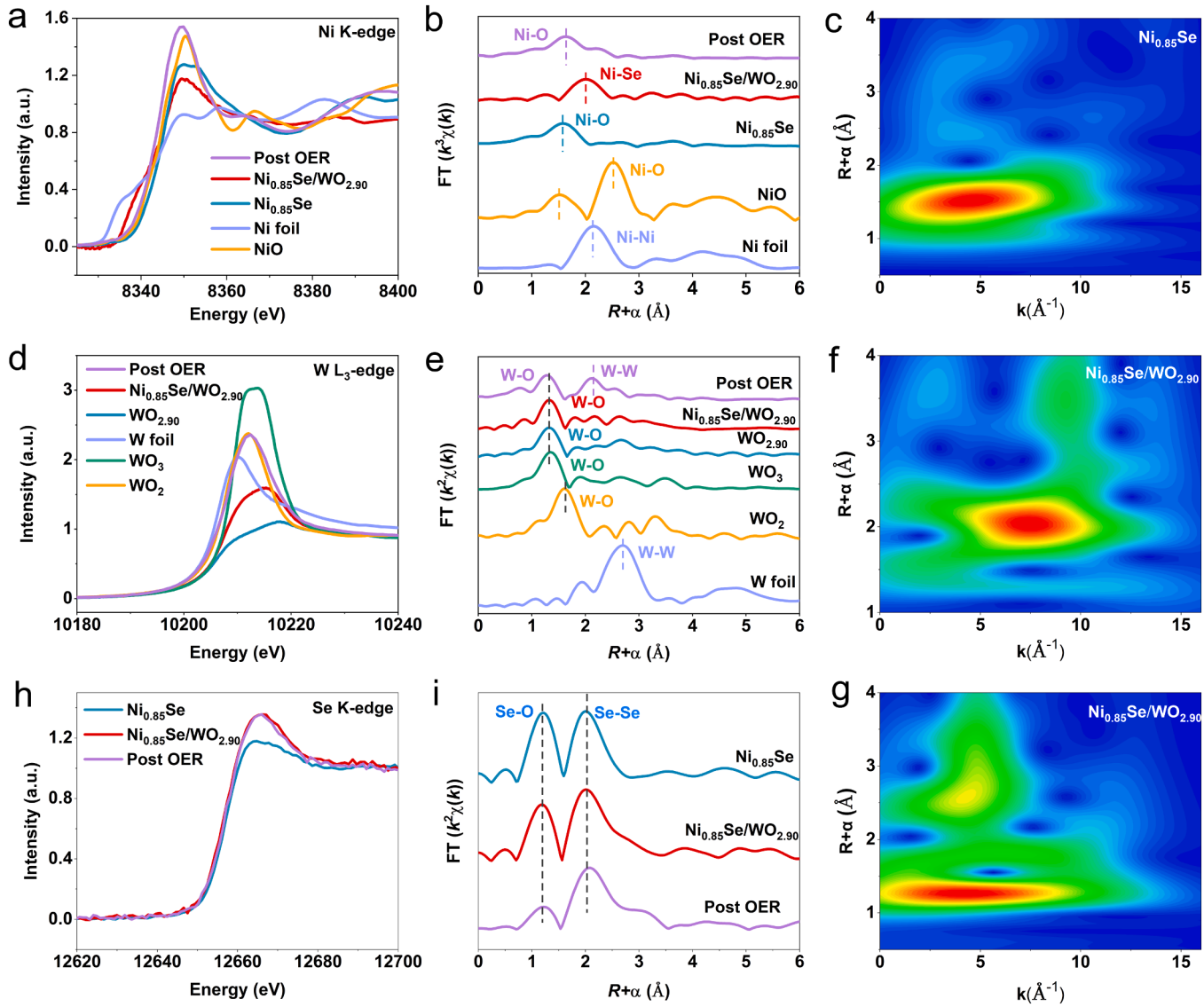

Fig. 3. (a) Normalized Ni K-edge XANES of $Ni_{0.85}Se/WO_{2.90}$ and post OER, $Ni_{0.85}Se$, Ni foil, and NiO. (b) The corresponding Fourier transformed k^3-weighted EXAFS spectra and (c, f) Wavelet transform of k^3-weighted EXAFS signals. (d) Normalized W L_3-edge XANES of $Ni_{0.85}Se/WO_{2.90}$ and post OER, $WO_{2.90}$, W foil, WO_2, and WO_3. (e) The corresponding Fourier transformed k^3-weighted EXAFS spectra. (g) Wavelet transform of k^3-weighted EXAFS signals.

indicates that the valence state of Ni is between 0 and + 2, in line with the XPS results. Notably, the absorption edge for $Ni_{0.85}Se/WO_{2.90}$ shifts noticeably toward the lower energy relative to that of $Ni_{0.85}Se$, implying the lower average Ni valence state (Fig. 3a). From the Ni K-edge fourier transforms EXAFS (FT-EXAFS) spectra, the dominant peaks of $Ni_{0.85}Se/WO_{2.90}$ are attributed to the scattering of Ni-Se (Fig. 3b). It can be clearly seen that the Ni-Se bond transforms into Ni-O bond post OER, which indicate that it gradually transforms into NiOOH during the OER process, which is consistent with the results of *in situ* Raman spectra. It is worth noting that compared to $Ni_{0.85}Se$, $Ni_{0.85}Se/WO_{2.90}$ has a shorter Ni-Ni bond length, which may be due to lattice distortion of the heterojunction at the interface. These results have also been confirmed in wavelet transform (WT) (Fig. 3c, f). The coordination configuration and atomic spacing were determined through quantitative least squares EXAFS curve fitting analysis. Compared with $Ni_{0.85}Se$, the lower Ni-Se coordination number (CN) of $Ni_{0.85}Se/WO_{2.90}$ confirms the presence of more oxygen vacancies and higher degree of disorder. As shown in the Fig. 3d-e, for the W-L_3 edge spectrum, the white line peak position of $Ni_{0.85}Se/WO_{2.90}$ is located at WO_2 (+4) and WO_3 (+6). Due to the increase of oxygen vacancies, its oxidation state is lower than that of the original $Ni_{0.85}Se$. Although the FT-EXAFS spectrum has almost the same peak position at the W-L_3 edge, the W-O intensity of $Ni_{0.85}Se/WO_{2.90}$ decreases, indicating that the CN coordinated by W-O is lower due to the effect of oxygen vacancies. In addition, the WT-EXAFS analysis of $Ni_{0.85}Se/WO_{2.90}$ provides higher radial distance resolution, further confirming the results of EXAFS, and Post OER, the W-W bonds were generated. As shown in Fig. 3h-i, analyzing the Se K edge of $Ni_{0.85}Se/WO_{2.90}$ before and post OER and $Ni_{0.85}Se$, it can be found that there is no

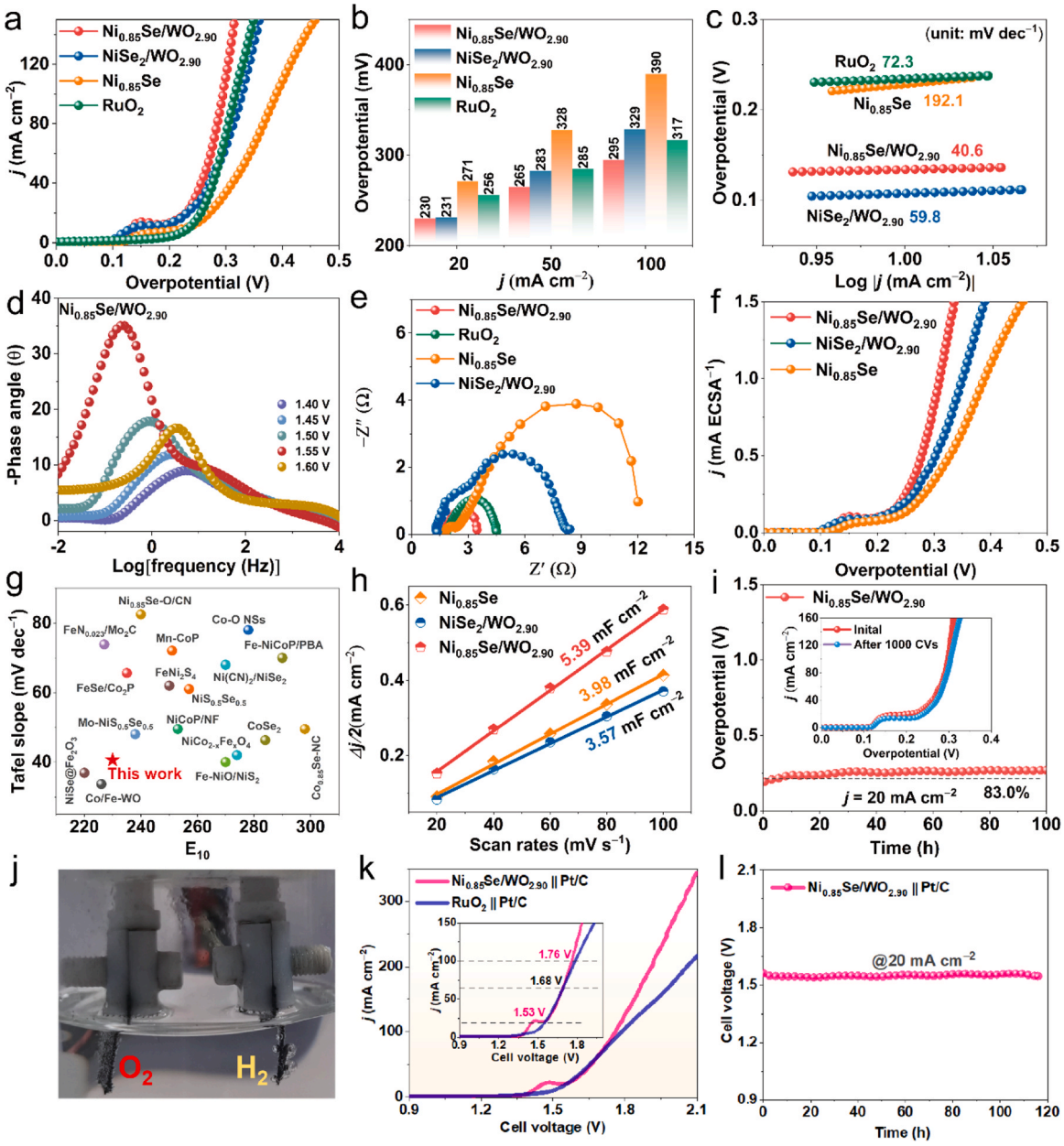

Fig. 4. Electrocatalytic performance of catalysts toward OER. (a) LSV polarization curves of $Ni_{0.85}Se/WO_{2.90}$, $NiSe_2/WO_{2.90}$, $Ni_{0.85}Se$, $WO_{2.90}$, and RuO_2. (b) Overpotentials at 10, 50, and 100 mA cm^{-2}. (c) Tafel plots. (d) Bode phase plots of $Ni_{0.85}Se/WO_{2.90}$. (e) EIS of the corresponding catalysts. (f) LSV curves of prepared catalysts normalized by the ECSA. (g) Comparison with the reported literature. (h) Double-layer capacitance (C_{dl}). (i) Chronopotentiometry curve of $Ni_{0.85}Se/WO_{2.90}$ at an applied current of 20 mA cm^{-2} for 100 h (insert: accelerated degradation test for 1000 cycles at a scan rate of 50 mV s^{-1}). (j) Photo of electrolyzed water. (k) Polarization plots of overall water splitting application in 1.0 M KOH. (l) Chronopotentiometry curve of $Ni_{0.85}Se/WO_{2.90}$||Pt/C at 20 mA cm^{-2}.

significant change in the valence state of Se. The corresponding FT EXAFS spectra suggest that the Se-Se coordination bond weakens post OER, indicating that it is gradually oxidized during the OER process.

3.2. Regulation of oxygen vacancies and lattice strain on electrocatalytic oxygen evolution

The electrochemical performance of the as-prepared sample-modified electrodes, in relation to the OER, was initially assessed in a 1.0 M KOH electrolyte. The linear sweep voltammetry (LSV) curve for $Ni_{0.85}Se/WO_{2.90}$ exhibits an oxidation peak around 1.38 V, likely due to the transition of Ni^{2+} to Ni^{3+} cations. As evident in Fig. 4a, the $Ni_{0.85}Se/WO_{2.90}$ electrode demands an overpotential at 20 mA cm^{-2} (η_{20}) of just 230 mV. This is significantly lower than the overpotentials of $Ni_{0.85}Se$ (271 mV), $WO_{2.90}$ (296 mV), $NiSe_2/WO_{2.90}$ (231 mV), and even the benchmark RuO_2 (256 mV) catalyst. Strikingly, for $Ni_{0.85}Se/WO_{2.90}$, the required overpotentials rise with the current densities: 265 mV at 50 mA cm^{-2} and 295 mV at 100 mA cm^{-2}, showcasing the outstanding OER activity of $Ni_{0.85}Se/WO_{2.90}$ (Fig. 4b). To delve deeper into the OER kinetics, we turn to the Tafel slopes extrapolated from the polarization curves (Fig. 4c). Here, $Ni_{0.85}Se/WO_{2.90}$ stands out, presenting the fastest kinetics with a minimal Tafel slope of 40.6 mV dec^{-1}. This is in stark contrast to $NiSe_2/WO_{2.90}$ (59.8 mV dec^{-1}), $Ni_{0.85}Se$ (192.1 mV dec^{-1}), and $WO_{2.90}$ (198.0 mV dec^{-1}), clearly emphasizing the superior OER kinetics of $Ni_{0.85}Se/WO_{2.90}$ in comparison to these control catalysts. With the increased applied potentials, the phase angles at low frequency for $Ni_{0.85}Se/WO_{2.90}$ show an accelerating trend of decline, indicating that the combination of $Ni_{0.85}Se$ and $WO_{2.90}$ can facilitate the electron transfer at electrolyte-catalyst interface and consequently lead to a superior OER kinetics (Fig. 4d).

Further experiments were conducted using catalysts prepared under varying conditions, including different temperatures, metal ratios, and an Ar-only calcination atmosphere. The outcomes, spanning from differing crystal structures to catalytic performances, uniformly suggest that $Ni_{0.85}Se/WO_{2.90}$ offers optimal OER activity (Figs. S14-16). It's hypothesized that the Ni component enhances the bridging oxygen site's activity, serving as a proton acceptor during the OER to expedite deprotonation and thus enhance kinetics. The enhanced performance of $Ni_{0.85}Se/WO_{2.90}$ over $NiSe_2/WO_{2.90}$ may be attributed to charge-transfer characteristics from $Ni_{0.85}Se$ to its growth template. Electrochemical impedance spectroscopy (EIS) was utilized to further verify charge-transfer kinetics. The charge-transfer resistance (R_{ct}) was derived from the semicircle's radius in the Nyquist plot's high-frequency domain. EIS results, as depicted in Fig. 4e and Fig. S17, demonstrate that R_{ct} values are ordered as $Ni_{0.85}Se/WO_{2.90}$ (1.4 Ω) < $NiSe_2/WO_{2.90}$ (4.8 Ω) < $Ni_{0.85}Se$ (7.8 Ω) = $WO_{2.90}$ (7.8 Ω) (Table S2). This suggests that an abundance of defects can ease interfacial charge transfer via intramolecular electron transfer [50]. Lastly, as highlighted in Fig. 4g and Table S3, the OER electrocatalytic activity demonstrated in this study surpasses many recently reported catalysts, both in terms of overpotential and Tafel slope.

The electrochemical surface area (ECSA), which is directly proportional to the double-layer capacitance (C_{dl}) of electrocatalyst, is a crucial parameter for understanding intrinsic activity. Cyclic voltammetry (CV) curves were recorded in the non-Faradaic region at various scan rates (Figs. S18-20). The calculated C_{dl} values for $Ni_{0.85}Se/WO_{2.90}$, $NiSe_2/WO_{2.90}$, $Ni_{0.85}Se$, and $WO_{2.90}$ were found to be 5.39, 5.39, 3.98, and 3.57 mF cm^{-2}, respectively (Fig. 4h). Furthermore, the ECSA values were calculated as 134.8, 99.5, and 89.3 cm^2 for $Ni_{0.85}Se/WO_{2.90}$, $NiSe_2/WO_{2.90}$, and $Ni_{0.85}Se$, respectively (Fig. S21). A larger ECSA indicates the exposure of more active sites, which is a significant contributing factor to the excellent performance of the material. To delve deeper into intrinsic catalytic activity, LSV curves were normalized to the ECSA. As anticipated, $Ni_{0.85}Se/WO_{2.90}$ exhibited the highest intrinsic activity, affirming that defects engineering and lattice strain effectively enhance the OER activity of $Ni_{0.85}Se/WO_{2.90}$ (Fig. 4f). The operational stability of electrocatalysts is crucial for evaluating their catalytic activity. A fast-degradation test, based on continuous CV cycling, was conducted (inset in Fig. 4i). There was only a slight decay in overpotential after 1000 CV cycles. Following a 100 h chronoamperometry test at 20 mA cm^{-2} (Fig. 4i), the $Ni_{0.85}Se/WO_{2.90}$ catalyst exhibited minimal voltage attenuation (17.0 %). It is presumed that the catalyst's voltage attenuation primarily results from catalyst detachment and structural collapse during continuous testing. Ex-situ characterization methods, including TEM, HRTEM, EDX, and XPS, were employed to assess the structural stability. Post-stability test TEM characterization revealed a morphology change to a transparent sheet containing small particles (Fig. S22a). HRTEM images indicated changes in lattice spacing, with 0.374 nm and 0.239 nm corresponding to the (110) plane of $WO_{2.90}$ and (011) plane of NiOOH, differing from the original 0.290 nm attributed to the (011) of $Ni_{0.85}Se$ (Fig. S22b). SAED patterns demonstrated reduced crystallinity, indicating changes on the catalyst surface (Fig. S22c). These TEM findings were consistent with in situ Raman results. After the long-term stability test, $Ni_{0.85}Se$ on the catalyst surface gradually evolved into NiOOH, confirming NiOOH as the real active site of the catalyst. Building upon the impressive OER capabilities of $Ni_{0.85}Se/WO_{2.90}$ catalyst, it was implemented as an anode in tandem with Pt/C as the cathode to form an electrolyzer ($Ni_{0.85}Se/WO_{2.90}$||Pt/C) designed for comprehensive water splitting. The experimental assembly utilizing a two-electrode configuration is depicted in Fig. 4j and Fig. S27a. For comparative analysis, a benchmark catalyst, RuO_2, was paired with Pt/C (RuO_2||Pt/C) and tested under identical conditions. The polarization curves for the assembled $Ni_{0.85}Se/WO_{2.90}$||Pt/C electrolyzer, shown in Fig. 4k, highlight its remarkable performance in overall water splitting. The electrolyzer achieved current densities of 20 and 100 mA cm^{-2} with a cell voltage requirement of just 1.53 V and 1.76 V, respectively. These results are competitive with the RuO_2||Pt/C pair, which required 1.52 V to achieve 20 mA cm^{-2}. It's significant to note that the $Ni_{0.85}Se/WO_{2.90}$||Pt/C electrolyzer outperforms the benchmark RuO_2||Pt/C, especially at elevated current densities. Comparatively, as seen in Fig. S27b and Table S4, the assembled electrolyzer demonstrates a significant edge in activity when benchmarked against other previously reported catalysts. Moreover, the long-term stability of the electrolyzer was assessed at a constant current density of 20 mA cm^{-2}. Fig. 4l shows a compelling operational stability for the electrolyzer. Even after rigorous testing for 120 h at 20 mA cm^{-2}, the cell voltage remained largely unchanged, attesting to its commendable performance in alkaline water electrolysis. All in all, these findings firmly establish $Ni_{0.85}Se/WO_{2.90}$ as a promising anode candidate for viable hydrogen production through water electrolysis.

3.3. Catalytic reaction pathway and activity analysis of OER process

Elemental analysis revealed a considerable dissolution of Se and a significant increase in oxygen content in the catalyst (Fig. S23). This indirectly indicated the formation of a substantial amount of NiOOH. XPS spectra demonstrated an increase in Ni^{3+} from 61.3 % to 82.5 % post OER, indicating more Ni cations becoming active OER sites (Fig. S22d and Fig. S23) [51]. The presence of Ni species in a high valence state is favorable for surface interactions between reaction intermediates and active sites, contributing to the superior OER activity [52].

Tracking the changes of intermediates during the OER is crucial for monitoring the reaction process and clarifying the pathway in real-time, a series of in-situ characterizations were conducted under actual OER working conditions to determine the key intermediates of reaction active sites. Firstly, the key reactions of intermediates in the OER process were detected using in-situ Fourier transform infrared (FTIR) spectroscopy to elucidate the mechanism of catalytic reactions. Under voltage, a clear peak was detected near 1108 cm^{-1} for $Ni_{0.85}Se/WO_{2.90}$ and $Ni_{0.85}Se$, representing the characteristic vibration of *OOH. In Fig. 5a, b, as the applied potential increases, the *OOH vibration band recorded by

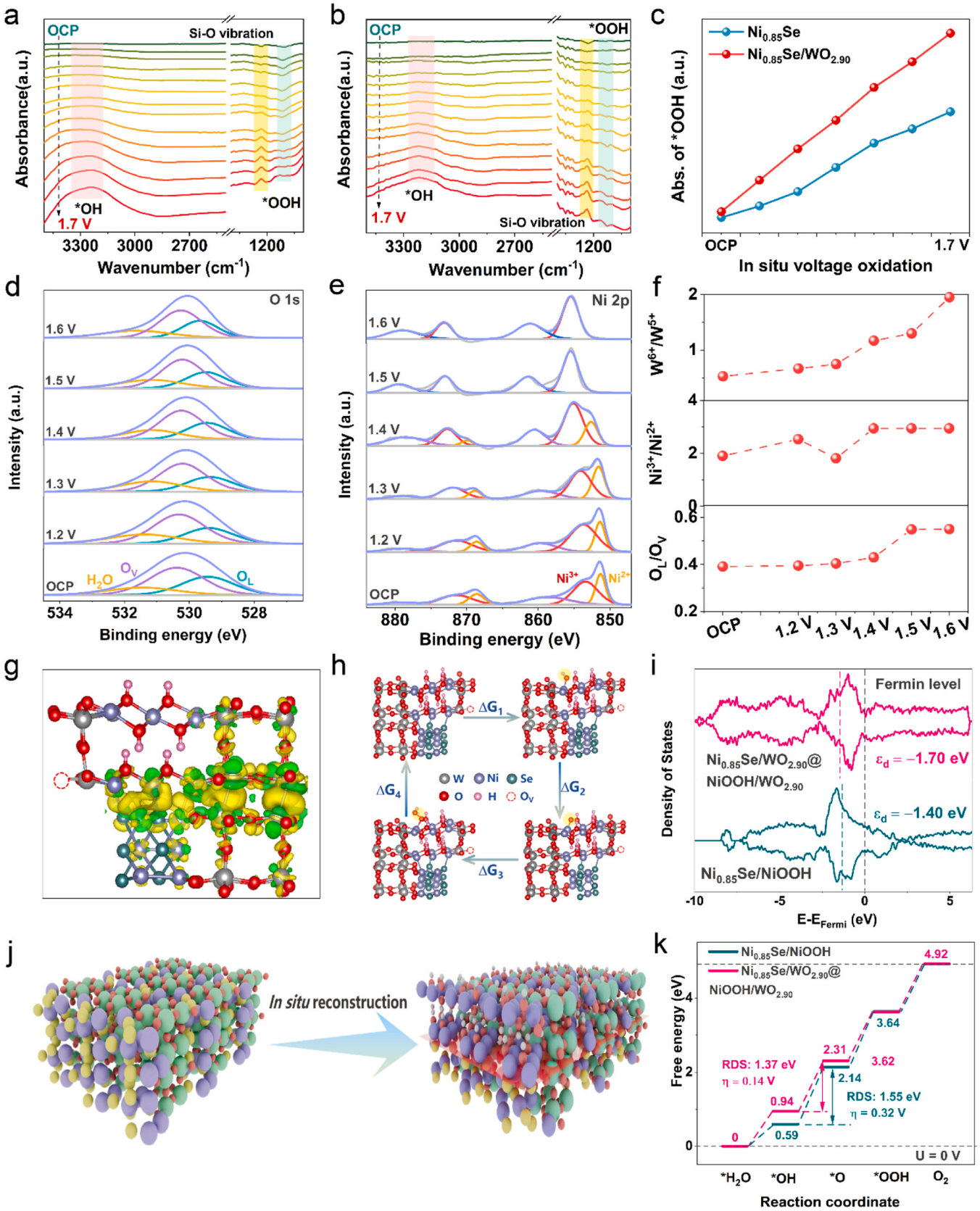

Fig. 5. In situ spectra of (a) $Ni_{0.85}Se$ and (b)$Ni_{0.85}Se/WO_{2.90}$. (c) Normalized intensity. (d) In situ O 1 s spectra and (e) Ni 2p spectra of $Ni_{0.85}Se/WO_{2.90}$. Variations in (f) W^{6+}/W^{5+}, Ni^{3+}/Ni^{2+}, and O_L/O_V. (g) The charge density difference for $Ni_{0.85}Se/WO_{2.90}$@NiOOH/$WO_{2.90}$, the yellow and green regions represent electron accumulation and depletion, respectively. (h) OER mechanism on $Ni_{0.85}Se/WO_{2.90}$@NiOOH/$WO_{2.90}$. (i) The density of states (DOS) of $Ni_{0.85}Se/WO_{2.90}$@NiOOH/$WO_{2.90}$ and $Ni_{0.85}Se$@NiOOH surfaces. (j) Schematic diagram of in situ reconstruction of catalyst in OER process (yellow, purple, green, red, and white balls represent Se, Ni, W, O, and H atoms, respectively). (k) Gibbs free energy profiles for OER on $Ni_{0.85}Se/WO_{2.90}$@NiOOH/$WO_{2.90}$ and $Ni_{0.85}Se$@NiOOH.

$Ni_{0.85}Se/WO_{2.90}$ is much stronger than that of $Ni_{0.85}Se$, indicating faster oxygen exchange on $Ni_{0.85}Se/WO_{2.90}$. In addition, *OH was detected at 3350 cm^{-1} (Fig. 5c). In order to gain a more comprehensive understanding of the dynamic structural changes of materials during operation, a series of XPS test results were collected at different potentials to monitor the elemental valence states and electronic structural changes of the materials. As shown in the Fig. 5d-f, detailed quantitative molecular analysis reveals a rapid increase in the relative percentage of Ni^{3+}/Ni^{2+} in $Ni_{0.85}Se/WO_{2.90}$, indicating the rapid formation of high valence active species, consistent with *in situ* Raman spectroscopy. The corresponding phenomenon is the O_L/O_V ratio of the O 1 s spectrum, and the graph shows the variation of the O_L/O_V ratio. The ratio of O_L/O_V can be used as a scale to estimate the relative number of surface oxygen vacancies. For $Ni_{0.85}Se/WO_{2.90}$, the relative content of O_L/O_V increased from 0.38 to 0.57, and the potential increased from OCP to 1.6 V, indicating that higher O_L values are beneficial for stabilizing the structure. For the W 4 f spectrum, as the voltage increases, the ratio of W^{6+}/W^{5+} gradually increases, indicating that the substrate of $WO_{2.90}$ plays a key role in stabilizing the $Ni_{0.85}Se/WO_{2.90}$ system.

To gain deeper insights into the high OER (oxygen evolution reaction) activity of the $Ni_{0.85}Se/WO_{2.90}$ heterostructure, density functional theory (DFT) calculations were conducted. To ensure the representation of the system, a complex $Ni_{0.85}Se/WO_{2.90}$@NiOOH/$WO_{2.90}$ structure was selected as the computational model. This model consists of the $Ni_{0.85}Se/WO_{2.90}$ surface covered with NiOOH/$WO_{2.90}$ material, aligning with the OER reaction process and supported by the results from in situ Raman and XPS/TEM post stability testing (Fig. S24) [26,53]. Charge density distribution in the $Ni_{0.85}Se/WO_{2.90}$@NiOOH/$WO_{2.90}$ heterostructure (Fig. 5g and Fig. S25) reveals intriguing patterns. Electrons are shown to accumulate around oxygen (O) atoms while depleting around nickel (Ni) and tungsten (W) atoms [2]. This illustrates the role of the heterostructure in adjusting the electronic structure of the material to improve its electrocatalytic performance. The alkaline OER reaction pathway involves four proton-electron steps, with the adsorption energies of intermediates (*OH, *O, and *OOH) on the active sites being crucial determinants of OER activity (Fig. 5h and Fig. S26). The density of states (DOS) analysis (Fig. 5i) demonstrates that forming a heterostructure with $WO_{2.90}$ significantly alters the electronic structure of Ni atoms, leading to a lower d-band center (ε_d) and improved conductivity and electron migration [54]. Lower ε_d values contribute to lower antibonding energy states and weakened interactions between adsorbed OH and the catalyst, ultimately accelerating OER kinetics. As depicted in Fig. 5j, the rate-determining step (RDS) for the Ni sites of $Ni_{0.85}Se$/-NiOOH is the deprotonation of *OH to *O with a Gibbs free energy of 1.55 eV (overpotential, η=0.32 V). In contrast, for $Ni_{0.85}Se/WO_{2.90}$@-NiOOH/$WO_{2.90}$, the RDS has a lower Gibbs free energy of 1.37 eV (η=0.14 V) [51]. This lower theoretical overpotential demonstrates a lower reaction barrier and aligns with the superior OER performance of the heterostructure. Besides, revealing that $WO_{2.90}$ could effectively regulate the energetics for OER intermediates. Fig. 5k shows the in-situ reconstruction mechanism of the catalyst under alkaline conditions, which better explains the reconstruction model.

In brief, the electrocatalyst achieved through this strategy offers several advantages: 1) Geometric stress caused by the replacement of atoms induces lattice distortion, increasing active sites. 2) Modification of $WO_{2.90}$ with $Ni_{0.85}Se$ optimizes the adsorption energy of reaction intermediates and reduces the OER catalytic barrier. 3) The structure enhances the local electric field and promotes the escape of generated gas, leading to significantly improved OER performance. This study sheds light on the enhancement mechanism of the catalyst's OER performance, highlighting its potential in practical applications.

4. Conclusions

In summary, the $Ni_{0.85}Se/WO_{2.90}$ heterostructure exhibits outstanding electrocatalytic performance for the OER. Its unique sea-urchin-like morphology increase defect sites, facilitating mass transport and exposing abundant active sites. And demonstrates exceptional stability evidenced by over 100 h with minimal voltage attenuation. The heterointerface induces significant lattice strain and abundant oxygen vacancies, effectively modulating the local electronic structure and promoting interfacial charge redistribution and delocalization, thereby reducing the Gibbs free energy of the rate-determining step. Combined experimental characterizations and first-principles calculations reveal that the built-in electric field at the interface facilitates charge transfer and optimizes the adsorption/desorption behavior of reaction intermediates, leading to significantly enhanced OER kinetics. Furthermore, in situ formed NiOOH serves as the active phase during operation, while W-O species contribute to structural stabilization. This work provides important theoretical and experimental insights for the atomic-level design of highly efficient heterostructured electrocatalysts.

CRediT authorship contribution statement

Tayirjan Taylor Isimjan: Methodology, Investigation. **Tianxiao Sun:** Methodology, Investigation. **Jianqiu Zhu:** Methodology, Investigation, Conceptualization. **Fengli Wei:** Methodology, Investigation. **Qimin Peng:** Writing – original draft, Methodology, Investigation, Conceptualization. **Bin Wu:** Writing – review & editing, Supervision, Methodology, Investigation, Funding acquisition, Formal analysis, Data curation, Conceptualization. **Xiulin Yang:** Writing – review & editing, Supervision, Methodology, Investigation, Funding acquisition, Conceptualization. **Yongfa Zhu:** Writing – review & editing, Visualization, Methodology, Investigation, Conceptualization.

Declaration of Competing Interest

The authors declare that they have no known competing financial interests or personal relationships that could have appeared to influence the work reported in this paper.

Acknowledgements

This work has been supported by the National Natural Science Foundation of China (no. 52363028, 21965005), Natural Science Foundation of Guangxi Province (2018GXNSFAA294077, 2021GXNSFAA076001), Innovation Project of Guangxi Graduate Education (YCBZ2025097), Guangxi Technology Base and Talent Subject (GUIKE AD23023004, GUIKE AD20297039) and the National Research Foundation, Singapore, and A*STAR (Agency for Science, Technology and Research) under its LCER Phase 2 Programme 1st Emerging Technology (Award No. U2411D4006) and Key Laboratory of Functional Inorganic Material Chemistry (Heilongjiang University), Ministry of Education, P. R. China. Key Laboratory of Applied Surface and Colloid Chemistry (Shaanxi Normal University), Ministry of Education, P. R. China.

Appendix A. Supporting information

Supplementary data associated with this article can be found in the online version at doi:10.1016/j.apcatb.2025.126158.

Data availability

Data will be made available on request.

References

[1] R. Liang, B. Zhang, Y. Du, X. Han, S. Li, P. Xu, Understanding the ANion Effect of Basic Cobalt Salts for the Electrocatalytic Oxygen Evolution Reaction, ACS Catal. 13 (2023) 8821–8829.

[2] C. Zhong, J. Zhang, L. Zhang, Y. Tu, H. Song, L. Du, Z. Cui, Composition-tunable $Co_{3-x}Fe_xMo_3N$ electrocatalysts for the oxygen evolution reaction, ACS Energy Lett. 8 (2023) 1455–1462.
[3] Q. Peng, Q. He, Y. Hu, T.T. Isimjan, R. Hou, X. Yang, Interface engineering of porous Fe_2P-$WO_{2.92}$ catalyst with oxygen vacancies for highly active and stable large-current oxygen evolution and overall water splitting, J. Energy Chem. 65 (2022) 574–582.
[4] L. Deng, S.-F. Hung, S. Liu, S. Zhao, Z.-Y. Lin, C. Zhang, Y. Zhang, A.-Y. Wang, H.-Y. Chen, J. Peng, R. Ma, L. Jiao, F. Hu, L. Li, S. Peng, Accelerated proton transfer in asymmetric active units for sustainable acidic oxygen evolution reaction, J. Am. Chem. Soc. 146 (2024) 23146–23157.
[5] H. Liu, H. Duan, J. Yu, C. Qiu, R. Yu, J. Gao, S. Li, X. Du, Z. Si, S. Yang, Strong electron coupling effect at the CoO/CeO_2 interface enables efficient oxygen evolution reaction, ACS Mater. Lett. 4 (2022) 2572–2578.
[6] Q. Lin, D. Guo, L. Zhou, L. Yang, H. Jin, J. Li, G. Fang, X. Chen, S. Wang, Tuning the interface of $Co_{1-x}S$/Co(OH)F by atomic replacement strategy toward high-performance electrocatalytic oxygen evolution, ACS Nano 16 (2022) 15460–15470.
[7] J.-C. Gan, L. Zhang, J.-J. Feng, Y.-C. Shi, X.-S. Li, A.-J. Wang, Self-supporting highly branched urchin-like NiCoP/NiFeP heterostructures as efficient bifunctional electrocatalyst for overall water splitting, J. Colloid Interface Sci. 687 (2025) 24–35.
[8] Y. Zhao, W. Wan, N. Dongfang, C.A. Triana, L. Douls, C. Huang, R. Erni, M. Iannuzzi, G.R. Patzke, Optimized NiFe-based coordination polymer catalysts: sulfur-tuning and operando monitoring of water oxidation, ACS Nano 16 (2022) 15318–15327.
[9] Q. Peng, X. Shao, C. Hu, Z. Luo, T. Taylor Isimjan, Z. Dou, R. Hou, X. Yang, Co_4S_3 grafted 1T-phase dominated WS_2 ultrathin nanosheet arrays for highly efficient overall water splitting in alkaline media, J. Colloid Interface Sci. 615 (2022) 577–586.
[10] Y. Chen, J. Xu, Y. Chen, L. Wang, S. Jiang, Z.H. Xie, T. Zhang, P. Munroe, S. Peng, Rapid defect engineering in FeCoNi/$FeAl_2O_4$ hybrid for enhanced oxygen evolution catalysis: a pathway to high-performance electrocatalysts, Angew. Chem. Int. Ed. 63 (2024) e202405372.
[11] J. Nai, X. Xu, Q. Xie, G. Lu, Y. Wang, D. Luan, X. Tao, X.W.D. Lou, Construction of $Ni(CN)_2$/$NiSe_2$ heterostructures by stepwise topochemical pathways for efficient electrocatalytic oxygen evolution, Adv. Mater. 1 (2021) 2104405.
[12] Y. Wang, X. Li, M. Zhang, J. Zhang, Z. Chen, X. Zheng, Z. Tian, N. Zhao, X. Han, K. Zaghib, Y. Wang, Y. Deng, W. Hu, Highly active and durable single-atom tungsten-doped $NiS_{0.5}Se_{0.5}$ nanosheet@$NiS_{0.5}Se_{0.5}$ Nanorod heterostructures for water splitting, Adv. Mater. 34 (2022) 2107053.
[13] F.T. Haase, A. Rabe, F.P. Schmidt, A. Herzog, H.S. Jeon, W. Frandsen, P. V. Narangoda, I. Spanos, K. Friedel Ortega, J. Timoshenko, T. Lunkenbein, M. Behrens, A. Bergmann, R. Schlogl, B. Roldan Cuenya, Role of nanoscale inhomogeneities in Co_2FeO_4 catalysts during the oxygen evolution reaction, J. Am. Chem. Soc. 144 (2022) 12007–12019.
[14] Z. Shi, J. Li, J. Jiang, Y. Wang, X. Wang, Y. Li, L. Yang, Y. Chu, J. Bai, J. Yang, J. Ni, Y. Wang, L. Zhang, Z. Jiang, C. Liu, J. Ge, W. Xing, Enhanced acidic water oxidation by dynamic migration of oxygen species at the Ir/Nb_2O_{5-x} catalyst/support interfaces, Angew. Chem. Int. Ed. 61 (2022) e202212341.
[15] J. Liu, J. Xiao, Z. Wang, H. Yuan, Z. Lu, B. Luo, E. Tian, G.I.N. Waterhouse, Structural and electronic engineering of Ir-doped Ni-(Oxy)hydroxide nanosheets for enhanced oxygen evolution activity, ACS Catal. 11 (2021) 5386–5395.
[16] X. Li, Q. Hu, H. Wang, M. Chen, X. Hao, Y. Ma, J. Liu, K. Tang, A. Abudula, G. Guan, Charge induced crystal distortion and morphology remodeling: Formation of Mn-CoP nanowire@Mn-CoOOH nanosheet electrocatalyst with rich edge dislocation defects, Appl. Catal. B Environ. 292 (2021) 120172.
[17] Y. Li, Y. Wu, H. Hao, M. Yuan, Z. Lv, L. Xu, B. Wei, In situ unraveling surface reconstruction of Ni_5P_4@FeP nanosheet array for superior alkaline oxygen evolution reaction, Appl. Catal. B Environ. 305 (2022) 121033.
[18] K. Chang, D.T. Tran, J. Wang, S. Prabhakaran, D.H. Kim, N.H. Kim, J.H. Lee, Atomic heterointerface engineering of Ni_2P-$NiSe_2$ nanosheets coupled znp-based arrays for high-efficiency solar-assisted water splitting, Adv. Funct. Mater. (2022) 2113224.
[19] L. Jiang, Y. Hao, M. Gu, L. Deng, Q. Chen, X. Zhang, L. Li, S. Peng, G. Wang, Manipulating charge distribution at organic-inorganic Interface via optimizing substituents for sustainable water electrolysis, Angew. Chem. Int. Ed. 64 (2025) e202423145.
[20] J. Diao, Y. Qiu, S. Liu, W. Wang, K. Chen, H. Li, W. Yuan, Y. Qu, X. Guo, Interfacial engineering of W_2N/WC heterostructures derived from solid-state synthesis: a highly efficient trifunctional electrocatalyst for ORR, OER, and HER, Adv. Mater. 32 (2020) 1905679.
[21] F. Li, Y. Li, L. Li, W. Luo, Z. Lu, X. Zhang, Z. Zheng, Heterostructured FeNi hydroxide for effective electrocatalytic oxygen evolution, Chem. Sci. 13 (2022) 9256–9264.
[22] J.-C. Gan, Z.-F. Jiang, K.-M. Fang, X.-S. Li, L. Zhang, J.-J. Feng, A.-J. Wang, Low Rh doping accelerated HER/OER bifunctional catalytic activities of nanoflower-like Ni-Co sulfide for greatly boosting overall water splitting, J. Colloid Interface Sci. 677 (2025) 221–231.
[23] J. Zhang, J. Qian, J. Ran, P. Xi, L. Yang, D. Gao, Engineering lower coordination atoms onto NiO/Co_3O_4 Heterointerfaces for boosting oxygen evolution reactions, ACS Catal. 10 (2020) 12376–12384.
[24] J. Lin, P. Wang, H. Wang, C. Li, X. Si, J. Qi, J. Cao, Z. Zhong, W. Fei, J. Feng, Defect-rich heterogeneous MoS_2/NiS_2 nanosheets electrocatalysts for efficient overall water splitting, Adv. Sci. 6 (2019) 1900246.
[25] Y. Yang, Y. Kang, H. Zhao, X. Dai, M. Cui, X. Luan, X. Zhang, F. Nie, Z. Ren, W. Song, An interfacial electron transfer on tetrahedral NiS_2/$NiSe_2$ heterocages with dual-phase synergy for efficiently triggering the oxygen evolution reaction, Small 16 (2020) 1905083.
[26] L. Zhang, J. Rong, Y. Yang, H. Zhu, X. Yu, C. Chen, H.M. Cheng, G. Liu, Activated FeS_2@NiS_2 core-shell structure boosting cascade reaction for superior electrocatalytic oxygen evolution, Small (2023) 2207472.
[27] X. Wang, G. Long, B. Liu, Z. Li, W. Gao, P. Zhang, H. Zhang, X. Zhou, R. Duan, W. Hu, C. Li, Rationally modulating the functions of Ni_3Sn_2-$NiSnO_x$ nanocomposite electrocatalysts towards enhanced hydrogen evolution reaction, Angew. Chem. Int. Ed. 62 (2023) e202301562.
[28] Y. Tong, H. Guo, D. Liu, X. Yan, P. Su, J. Liang, S. Zhou, J. Liu, G.Q.M. Lu, S.X. Dou, Vacancy engineering of iron-doped $W_{18}O_{49}$ nanoreactors for low-barrier electrochemical nitrogen reduction, Angew. Chem. Int. Ed. 59 (2020) 7356–7361.
[29] Z. Xi, J. Li, D. Su, M. Muzzio, C. Yu, Q. Li, S. Sun, Stabilizing CuPd nanoparticles via CuPd coupling to $WO_{2.72}$ nanorods in electrochemical oxidation of formic acid, J. Am. Chem. Soc. 139 (2017) 15191–15196.
[30] M. Chen, Y. Zhang, R. Wang, B. Zhang, B. Song, Y. Guan, S. Li, P. Xu, Surface reconstruction of Se-doped NiS_2 enables high-efficiency oxygen evolution reaction, J. Energy Chem. 84 (2023) 173–180.
[31] H. Zhong, Q. Zhang, J. Yu, X. Zhang, C. Wu, Y. Ma, H. An, H. Wang, J. Zhang, X. Wang, J. Xue, Fundamental understanding of structural reconstruction behaviors in oxygen evolution reaction electrocatalysts, Adv. Energy Mater. (2023) 2301391.
[32] Z. Yang, F. Lai, Q. Mao, C. Liu, S. Peng, X. Liu, T. Zhang, Breaking the mutual-constraint of bifunctional oxygen electrocatalysis via Direct O—O coupling on high-valence Ir single-atom on MnOx, Adv. Mater. 37 (2024) 2412950.
[33] Y. Zhao, Q. Wen, D. Huang, C. Jiao, Y. Liu, Y. Liu, J. Fang, M. Sun, L. Yu, Operando reconstruction toward dual-cation-defects co-containing NiFe oxyhydroxide for ultralow energy consumption industrial water splitting electrolyzer, Adv. Energy Mater. 13 (2023) 2203595.
[34] X. Liu, J. Wang, H. Liao, J. Chen, S. Zhang, L. Tan, X. Zheng, D. Chu, P. Tan, J. Pan, Cationic oxidative leaching engineering modulated in situ self-reconstruction of nickel sulfide for superior water oxidation, Nano Lett. 23 (2023) 5027–5034.
[35] S. Zhao, F. Hu, L. Yin, L. Li, S. Peng, Manipulating electron redistribution induced by asymmetric coordination for electrocatalytic water oxidation at a high current density, Sci. Bull. 68 (2023) 1389–1398.
[36] J. Park, S. Lee, H.E. Kim, A. Cho, S. Kim, Y. Ye, J.W. Han, H. Lee, J.H. Jang, J. Lee, Investigation of the Support Effect in Atomically Dispersed Pt on WO_{3-x} for Utilization of Pt in the Hydrogen Evolution Reaction, Angew. Chem. Int. Ed. 58 (2019) 16038–16042.
[37] H. Yu, M. Hu, C. Chen, C. Hu, Q. Li, F. Hu, S. Peng, J. Ma, Ambient γ-Rays-Mediated Noble-Metal Deposition on Defect-Rich Manganese Oxide for Glycerol-Assisted H_2 Evolution at Industrial-Level Current Density, Angew. Chem. Int. Ed. 62 (2023) e202314569.
[38] T. Li, H.C. Fu, X.H. Chen, F. Gu, N.B. Li, H.Q. Luo, Interface engineering of core-shell $Ni_{0.85}Se$/NiTe electrocatalyst for enhanced oxygen evolution and urea oxidation reactions, J. Colloid Interface Sci. 618 (2022) 196–205.
[39] Z. Shen, Z. Zhao, J. Wen, J. Qian, Z. Peng, X. Fu, Role of Oxygen Vacancies in the Electrical Properties of WO_{3-x} Nano/Microrods with Identical Morphology, J. Nanomater 2018 (2018) 1–12.
[40] X. Zheng, M. Qin, S. Ma, Y. Chen, H. Ning, R. Yang, S. Mao, Y. Wang, Strong oxide-support interaction over IrO_2/V_2O_5 for efficient ph-universal water splitting, Adv. Sci. 9 (2022) 2104636.
[41] S. Anantharaj, E. Subhashini, K.C. Swaathini, T.S. Amarnath, S. Chatterjee, K. Karthick, S. Kundu, Respective influence of stoichiometry and NiOOH formation in hydrogen and oxygen evolution reactions of nickel selenides, Appl. Surf. Sci. 487 (2019) 1152–1158.
[42] Y. Wang, Q. Lu, F. Li, D. Guan, Y. Bu, Atomic-scale configuration enables fast hydrogen migration for electrocatalysis of acidic hydrogen evolution, Adv. Funct. Mater. (2023) 2213523.
[43] Y. Liu, Y. Zheng, D. Feng, L. Zhang, L. Zhang, X. Song, Z.A. Qiao, Efficient selective oxidation of aromatic alkanes by double cobalt active sites over oxygen vacancy-rich mesoporous Co_3O_4, Angew. Chem. Int. Ed. (2023) e202306261.
[44] Y. Wang, L. Li, G. Li, Q. Zhao, Xs Wu, Y. Wang, Y. Sun, C. Hu, Synergy of oxygen vacancies and Ni^0 species to promote the stability of a Ni/ZrO_2 catalyst for dry reforming of methane at low temperatures, ACS Catal. 13 (2023) 6486–6496.
[45] M. Ning, F. Zhang, L. Wu, X. Xing, D. Wang, S. Song, Q. Zhou, L. Yu, J. Bao, S. Chen, Z. Ren, Boosting efficient alkaline fresh water and seawater electrolysis via electrochemical reconstruction, Energy Environ. Sci. 15 (2022) 3945–3957.
[46] T. Kang, K. Kim, M. Kim, J. Kim, Synergistic metal-oxide interaction for efficient self-reconstruction of cobalt oxide as highly active water oxidation electrocatalyst, J. Catal. 404 (2021) 80–88.
[47] B. Wu, S. Gong, Y. Lin, T. Li, A. Chen, M. Zhao, Q. Zhang, L. Chen, A Unique NiOOH@FeOOH Heteroarchitecture for Enhanced Oxygen Evolution in Saline Water, Adv. Mater. (2022) 2108619.
[48] Y. Lin, J. Fang, W. Wang, Q. Wen, D. Huang, D. Ding, Z. Li, Y. Liu, Y. Shen, T. Zhai, Operando Reconstructed Molecule Fence to Stabilize NiFe-Based Oxygen Evolution Catalysts, Adv. Energy Mater. (2023) 2300604.
[49] K. Guo, H. Li, J. Huang, Y. Wang, Y. Peng, S. Lu, C. Xu, Selenization triggers deep reconstruction to produce ultrathin γ-NiOOH toward the efficient water oxidation, J. Energy Chem. 63 (2021) 651–658.
[50] Y. Li, W. Wang, M. Cheng, Y. Feng, X. Han, Q. Qian, Y. Zhu, G. Zhang, Arming Ru with Oxygen-Vacancy-Enriched RuO_2 Sub-Nanometer Skin Activates Superior Bifunctionality for pH-Universal Overall Water Splitting, Adv. Mater. (2023) 2206351.

[51] T.T. Yin, H.M. Xu, X.L. Zhang, X. Su, L. Shi, C. Gu, S.K. Han, Mn-Incorporation-Induced Phase Transition in Bottom-Up Synthesized Colloidal Sub-1-nm $Ni(OH)_2$ Nanosheets for Enhanced Oxygen Evolution Catalysis, Nano Lett. 23 (2023) 3259–3266.

[52] J.-T. Ren, L. Chen, H.-Y. Wang, W.-W. Tian, X.-L. Song, Q.-H. Kong, Z.-Y. Yuan, Synergistic activation of crystalline Ni_2P and amorphous $NiMoO_x$ for efficient water splitting at high current densities, ACS Catal. 13 (2023) 9792–9805.

[53] S.F. Zai, X.Y. Gao, C.C. Yang, Q. Jiang, Ce-modified $Ni(OH)_2$ nanoflowers supported on $NiSe_2$ octahedra nanoparticles as high-efficient oxygen evolution electrocatalyst, Adv. Energy Mater. 11 (2021) 2101266.

[54] J. Li, C. Hou, C. Chen, W. Ma, Q. Li, L. Hu, X. Lv, J. Dang, collaborative interface optimization strategy guided ultrafine RuCo and MXene heterostructure electrocatalysts for efficient overall water splitting, ACS Nano 17 (2023) 10947–10957.